

## Effect of Catalyst Bed Arrangement on the Conversion of Processed Palm Oil into Bio-Jet Fuel Using Co/ZSM-5 Catalyst

Pangestu Arum Pratiwi<sup>1</sup>, Triyono Triyono<sup>1\*</sup>, Wega Trisunaryanti<sup>1</sup>,  
Adyatma Bhagaskara<sup>1,2</sup>, and Dita Adi Saputra<sup>2</sup>

<sup>1</sup>Department of Chemistry, Faculty of Mathematics and Natural Sciences, Universitas Gadjah Mada, Sekip Utara, Yogyakarta 55281, Indonesia

<sup>2</sup>Research Center for Conversion and Energy Conservation, National Research and Innovation Agency (BRIN), KST BJ Habibie, Serpong, Tangerang Selatan 15310, Indonesia

\* **Corresponding author:**

email: triyn102@ugm.ac.id

Received: October 5, 2025

Accepted: December 4, 2025

DOI: 10.22146/ijc.111796

**Abstract:** The growing demand for sustainable aviation fuels has driven the development of efficient catalyst materials. This study aimed to investigate the physicochemical properties of the Co/ZSM-5 catalyst, evaluate the effect of catalyst bed arrangement (single- and double-bed configurations) on catalytic performance, and assess its reusability for converting processed palm oil into bio-jet fuel. The catalyst was analyzed using XRD, FTIR, Raman, SAA, NH<sub>3</sub>-TPD, XPS, and SEM-EDX instruments. The experiment was conducted in a semi-batch reactor equipped with a dual furnace. The hydrotreatment process was carried out at temperatures ranging from 200 to 550 °C with an H<sub>2</sub> flow rate of 20 mL/min for 3 h. The liquid product was analyzed by GC-MS and FTIR, while the spent catalyst was characterized by SEM-EDX mapping. The results showed that the catalyst exhibited good crystallinity, a moderate surface area, a suitable pore structure, strong acidity, and a stable cobalt dispersion. Catalyst activity tests revealed bio-jet fuel yields of 48.17% for the single-bed Co/ZSM-5 catalyst and 51.74% for the double-bed arrangement, highlighting the significant influence of bed arrangement effect on product yield and selectivity. After three reusability cycles, both single- and double-bed Co/ZSM-5 catalysts demonstrated consistent yields with relatively stable selectivity.

**Keywords:** bed arrangement; bio-jet fuel; Co/ZSM-5; hydrotreatment; processed palm oil

### ■ INTRODUCTION

The aviation sector has a high demand for fuel, predominantly derived from non-renewable fossil fuels. In Indonesia, fossil fuel reserves are being progressively depleted in line with increasing consumption, raising concerns about a potential energy crisis. The increase in fossil fuel consumption significantly increases atmospheric carbon emissions, which ultimately affects the environment, including global warming [1]. Aviation turbine fuel (ATF) is a petroleum product specifically designed for aircraft use, with the main component being a hydrocarbon chain containing a range of carbon atoms from C6 to C7 [2]. The Director of PT Pertamina Patra Niaga reported that Indonesia's avtur consumption has reached 5.72 million kL and is projected to rise by 10.7%

in 2024. Addressing this issue requires transitioning from conventional fossil fuels to alternative aviation fuels that can reduce CO<sub>2</sub>, SO<sub>x</sub>, and NO<sub>x</sub> emissions while supporting sustainable energy development, such as bio-jet fuel.

Bio-jet fuel can be produced by converting vegetable oils, such as refined palm oil, which is a derivative of palm oil known as shortening. The shortening is a refined derivative of palm kernel oil and is highly stable against oxidation [3]. Shortening, which contains high levels of fatty acids, can be converted into biofuel via esterification or hydrotreatment for bio-jet fuel production [4]. Its fatty acid composition is primarily dominated by myristic (C<sub>14</sub>), palmitic (C<sub>16</sub>), and oleic (C<sub>18</sub>) acids, which undergo hydrogenation, hydrocracking, and hydrodeoxygenation to yield hydrocarbons suitable as bio-jet fuel components.

The conversion of shortening into bio-jet fuel was achieved through a hydrotreatment process, which involved hydrotreating, hydrodeoxygenation, decarbonylation, decarboxylation, and hydrocracking [4]. The hydrocracking reaction requires temperatures exceeding 400 °C to break down large molecules into smaller ones, whereas the hydrodeoxygenation reaction can occur within a temperature range of 250–450 °C and at high pressures around 10–300 atm [5]. The presence of hydrogen required in hydrotreatment can suppress the emergence of sulfur, nitrogen, and oxygen from oil. The by-product of the hydrotreatment process is coke, which can degrade product quality. Coke can be minimized by adding a catalyst during the hydrocracking process [6].

Bifunctional catalysts are employed in the hydrotreatment process of converting white oil into bio-jet fuel, which involves combining acid sites for hydrocracking and metal sites for hydrogenation. Acid catalysts are used for their high catalytic activity and thermal stability. Acid catalysts have high efficiency for the cracking and isomerization pathways in the hydroprocess [7]. Zeolite Socony Mobile-5 (ZSM-5) is classified as an acid catalyst and features an effective pore structure during catalytic reactions [8]. The catalyst can filter molecules by selectively trapping some and allowing others to pass through, thanks to its porous structure. The performance of the ZSM-5 catalyst can be enhanced by the addition of a metal. Transition metals, such as platinum (Pt), palladium (Pd), and ruthenium (Ru), are widely used as catalysts due to their excellent activity and product selectivity. However, these metals are expensive and therefore less suitable for industrial applications. Cobalt (Co) can be used as an alternative to precious metals due to its relatively low price, abundant availability, and comparable stability to precious-metal catalysts [9-10]. Co has empty *d* orbitals, which can play a role in hydrocracking and hydrodeoxygenation reactions. The modification of the ZSM-5 catalyst with Co metal successfully increased the yield of crude oil and gas bio compared to the treatment without a catalyst [11].

Co metal can be dispersed on the carrier surface through an impregnation method. Spray impregnation is often used in catalyst preparation because it has a short

process, a high success rate, produces less waste, and evenly distributes the metal active sites. The spray impregnation method for the Mo/HZSM-5 catalyst has proven successful in converting refined palm kernel oil (RPKO) into bioavtur [4]. In addition to impregnation methods, ultrasonic waves can be used for catalyst preparation. The effect of acoustic cavitation in sonication creates a homogeneous contact between the metal and the carrier, thereby enhancing and maintaining catalytic activity [12]. This study will prepare the Co/ZSM-5 catalyst using a spray impregnation method followed by ultrasonic waves. The catalyst will be tested in two configurations: a single-bed and a double-bed. Catalyst reusability testing will be conducted to determine the catalyst's effectiveness in converting refined palm oil into bio-jet fuel. A novelty in this study is the metal impregnation process, which utilizes ultrasonic waves, and the use of refined palm oil as feedstock in the form of shortening.

## ■ EXPERIMENTAL SECTION

### Materials

The materials used in this study were vegetable oil, specifically in the form of shortening (white butter), as bait. The catalyst used in this study was the ZSM-5 catalyst (Meiqi Industry & Trade Co., Ltd., Si/Al = 50). The chemicals used were deionized water (CV Bima Aksara Nusa), cobalt(II) nitrate hexahydrate ( $\text{Co}(\text{NO}_3)_2 \cdot 6\text{H}_2\text{O}$ , Merck p.a.), hydrogen gas (PT Surya Indotim Imex), and nitrogen gas (PT Surya Indotim Imex).

### Instrumentation

The instruments used were X-ray diffractometer (PANanalytical Empyrean), temperature programmed desorption of ammonia (TPD-NH<sub>3</sub>, Micrometrics Chemisorb 2750), sonicator (Biobase UCD-150), Fourier-transform infrared (FTIR, Thermo Scientific Nicolet iS10), scanning electron microscope with energy dispersive X-ray (JEOL model JSM-6510LA), surface area analyzer (Quantachrome NovaWin), X-ray photoelectron spectrometer (XPS, Shimadzu), Raman spectroscopy (Thermoscientific), and gas chromatography-mass spectrometry (Shimadzu

QP2010S). The reactor used in this study was a semi-batch stainless steel reactor with a one-pot dual heater system.

## Procedure

### Preparation of Co/ZSM-5 by impregnation followed by sonication

Co metal was loaded onto ZSM-5 using the dry-spray impregnation method, followed by sonication. The precursor of Co as the metal to be loaded onto the ZSM-5 catalyst was obtained from  $\text{Co}(\text{NO}_3)_2 \cdot 6\text{H}_2\text{O}$ . The amount of Co metal precursor to be used must be calculated first based on Eq. (1).

$$\text{Precursor mass } (\text{Co}(\text{NO}_3)_2 \cdot 6\text{H}_2\text{O}) = \frac{\text{Mr cobalt(II) hexahydrate}}{\text{IArCo}} \times C \times m_p \quad (1)$$

The description of Eq. (1) refers to the concentration of Co/HZSM-5 metal, with a Co content of 6%, and the mass of ZSM-5 carrier in grams, specified as 1 g. The precursor of Co metal, as much as 0.2963 g, was dissolved in 3 mL of deionized water so that the ratio used between Co metal and deionized water is 1:3. The dissolved Co metal was then impregnated into the ZSM-5 carrier material by spraying and stirring until the catalyst paste (slurry) was formed. After that, the catalyst paste was placed in a sonicator for 45 min at 90 W, corresponding to approximately 60% power. The catalyst paste is dried in an oven at 110 °C for 2 h and then calcined for 3 h. Calcination was carried out at a flow rate of 20 mL/min of  $\text{N}_2$  gas at 500 °C. After that, the catalyst was reduced with hydrogen gas at a flow rate of 20 mL/min for 3 h at the same temperature. The fresh catalyst was analyzed using XRD, FTIR, Raman, SAA,  $\text{NH}_3$ -TPD, XPS, and SEM-EDX.

### Application of the catalyst in the reactor through the hydrotreatment process

The synthesized catalyst was tested in a semi-batch reactor equipped with a dual-furnace system and various catalyst arrangements. The application process involved three stages: thermal cracking, catalytic cracking, and hydrotreating. Thermal testing was first conducted to evaluate reactor performance by heating the feed container to 200–550 °C without a catalyst, increasing the temperature by 25 °C every 13 min. The first liquid drop obtained was considered the thermal cracking point, after

which hydrogen gas was introduced at a flow rate of 20 mL/min for 3 h. A feed of 100 mL was processed, and the resulting liquid products collected within the 200–550 °C fraction were analyzed. Catalytic cracking was then carried out using the ZSM-5 catalyst at 200 °C under similar conditions, with the products measured and characterized by GC-MS and FTIR.

The activity of the Co/ZSM-5 catalyst was further examined through hydrotreatment using both single- and double-bed configurations. In this stage, 100 g of shortening feed was placed in the upper sleeve, and 1 g of catalyst was loaded into the reactor, maintaining a catalyst-to-feed weight ratio of 1:100 (w/w). Hydrogen gas was continuously supplied at a rate of 20 mL/min for 3 h, while the reactor temperature was maintained between 200 and 550 °C. The same procedure was repeated with a double-bed catalyst arrangement to evaluate its performance under identical conditions.

### Catalyst reusability test

Catalysts with both arrangements, namely single- and double-bed catalysts, were re-run in the reactor three times. The reactor scheme is shown in Fig. 1. The hydrotreatment process was carried out using the same catalyst, with a feed rate of 20 mL/min. The liquid fraction product was collected over the same temperature range, 200–550 °C. All liquid product samples were analyzed by GC-MS, and the optimal catalyst arrangement was identified by FTIR. Spent catalyst was analyzed by SEM-EDX mapping. Conversion of liquid products, selectivity, and yield of bio jet fuel compounds, oxygenate compounds, and non-bio-jet fuel hydrocarbon compounds can be determined using Eq. (2–7);

$$\text{Liquid product conversion (\% w / w)} = \frac{W_{pc}}{W_{feed}} \times 100\% \quad (2)$$

where  $W_{pc}$  represents the mass of the liquid product obtained from the hydrodeoxygenation (HDO) process (g), while  $W_{feed}$  denotes the mass of the feed introduced into the HDO process (g).

$$\text{Yield of bio-jet fuel compound (\% w / w)} = \frac{A_b}{A_t} \times \frac{W_{pc}}{W_{feed}} \times 100\% \quad (3)$$

$$\text{Yield of oxygenated compound (\% w / w)} = \frac{A_o}{A_t} \times \frac{W_{pc}}{W_{feed}} \times 100\% \quad (4)$$

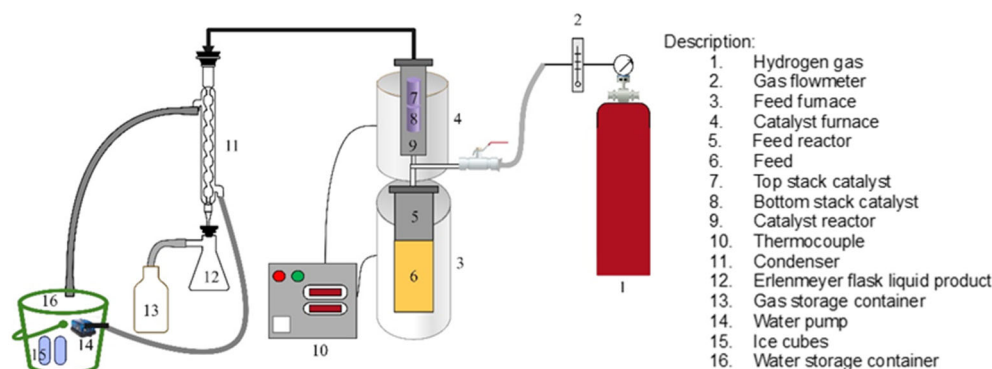


Fig 1. Semi-batch stainless steel reactor with dual heaters in a one-pot system

$$\text{Yield of non bio-jet fuel compound (\%w/w)} = \frac{A_n}{A_t} \times \frac{W_{pc}}{W_{feed}} \times 100\% \quad (5)$$

$$\text{Yield of main bio-jet fuel compound (\%w/w)} = \frac{A_{bp}}{A_t} \times \frac{W_{pc}}{W_{feed}} \times 100\% \quad (6)$$

$$\text{Selectivity (\%)} = \frac{\text{Area of specific fraction}}{\text{Total area of all compounds}} \times 100\% \quad (7)$$

$A_b$  is the percentage area of bio-jet fuel compounds in the GC spectra (%area),  $A_o$  denotes the percentage area of oxygenated compounds in the GC spectra (%area),  $A_n$  represents the percentage area of non-bio-jet fuel compounds in the GC spectra (%area),  $A_{bp}$  corresponds to the percentage area of main bio-jet fuel compounds in the GC spectra (%area), and  $A_t$  is the total percentage area in the GC spectra (%area). Meanwhile,  $W_{pc}$  refers to the mass of the liquid product obtained from the HDO process (g), and  $W_{feed}$  denotes the feed mass used in the HDO process (g).

After reusability testing, the three liquid products resulting from hydrotreatment with the best catalyst composition are mixed. The resulting fractions will be separated by distillation at a maximum temperature of 150 °C. The resulting distillation product will be tested according to ASTM D7566, which includes measurements of freezing point, kinematic viscosity, dynamic viscosity, density, and API gravity.

## ■ RESULTS AND DISCUSSION

### Catalyst Characterization

#### *Diffractogram analysis of ZSM-5 and Co/ZSM-5 catalysts*

As shown in Fig. 2, both ZSM-5 and Co/ZSM-5 catalysts exhibit crystalline structures, confirmed by the

sharp peaks in their XRD patterns. The peaks of ZSM-5 appear sharper than those of Co/ZSM-5, indicating reduced crystallinity due to Co species partially covering the ZSM-5 framework. Crystallite sizes were determined from the XRD data using the Debye–Scherrer equation, where the full width at half maximum (FWHM) is inversely proportional to crystallite size. The peak broadening in the Co/ZSM-5 diffractogram indicates that the presence of cobalt and the cavitation impact of ultrasonic treatment contributed to a reduction in crystallite size. The crystallinity and average crystallite sizes are summarized in Table 1.

The diffractogram in Fig. 2 confirms that the ZSM-5 catalyst exhibits the typical MFI structure, indicated by the 2θ diffraction peaks corresponding to SiO<sub>2</sub> minerals (COD 96–154–8625). The dominant phase in the ZSM-5

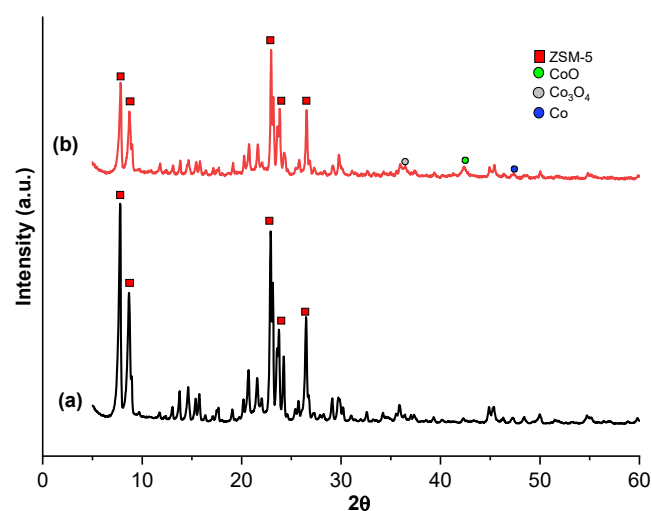


Fig 2. Diffractograms of catalysts (a) ZSM-5 and (b) Co/ZSM-5

**Table 1.** Degree of crystallinity and average crystal size with Debye Scherrer

Catalyst	Degree of crystallinity (%)	Average crystal size (nm)
ZSM-5	76.14	22.23
Co/ZSM-5	74.16	20.94

support is  $\text{Al}_2\text{SiO}_5$ , consistent with the COD database (96–900–6530). For the Co/ZSM-5 catalyst, the main compounds identified are  $\text{Co}_3\text{O}_4$  (COD 96–591–0032), Co (COD 96–901–1616), and CoO (COD 96–153–3088). The coexistence of  $\text{Co}_3\text{O}_4$  and CoO suggests incomplete reduction, likely due to strong interactions between cobalt oxides and the ZSM-5 surface that hinder  $\text{H}_2$  dissociation, as well as the relatively large particle size of cobalt oxides, which restricts hydrogen diffusion. Furthermore, the 2 $\theta$  shift observed after cobalt impregnation is attributed to the appearance of overlapping peaks from cobalt oxide phases.

#### FTIR spectra analysis of ZSM-5 and Co/ZSM-5 catalysts

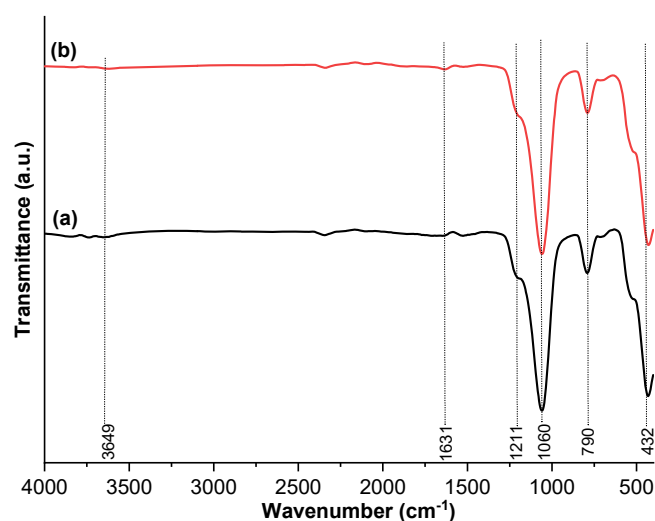
Based on Fig. 3, the IR spectra of Co/ZSM-5 exhibit a new absorption at  $1631\text{ cm}^{-1}$ , corresponding to O–Co–O vibrations, which confirms the successful incorporation of cobalt into the ZSM-5 framework. The presence of this band also indicates the formation of Lewis acid sites, as Co species with vacant orbitals act as electron acceptors [15]. Importantly, Co impregnation did not significantly alter the functional groups of ZSM-5.

The characteristic vibrations of ZSM-5, including tetrahedral Si/Al bending, symmetric and asymmetric Si–O/Al–O stretching, and H–O–H bending, were still observed. However, the peak intensities at  $3649\text{ cm}^{-1}$  (–OH stretching) and  $1060\text{ cm}^{-1}$  (H–O–H bending) decreased due to calcination, which removed water molecules at high temperature. Asymmetric stretching

vibrations ( $1211\text{ cm}^{-1}$ ) appeared at higher wavenumbers than symmetric ones ( $790\text{ cm}^{-1}$ ), reflecting greater dipole moment changes and higher energy requirements. These FTIR results for both ZSM-5 and Co/ZSM-5 are summarized in Table 2.

#### Raman spectra analysis of ZSM-5 and Co/ZSM-5 catalysts

Based on the Raman spectroscopy results presented in Fig. 4, a new peak appears in Fig.4(b) and corresponds to Co/ZSM-5. The new peaks appear at  $475$  and  $679\text{ cm}^{-1}$  in the Raman spectrum. Co species can be present in the  $450\text{--}700\text{ cm}^{-1}$  zone, which is a characteristic

**Fig 3.** FTIR spectra of catalysts (a) ZSM-5 and (b) Co/ZSM-5**Table 2.** FTIR spectra interpretation of ZSM-5 and Co/ZSM-5 catalysts

Wavenumber ( $\text{cm}^{-1}$ )		Type of vibration	Reference
ZSM-5	Co/ZSM-5		
432	432	Binding vibration T–O	[13]
790	790	Stretching symmetric vibration T–O	[14]
1060	1060	Binding vibration H–O–H	[15]
1211	1211	Stretching asymmetric vibration T–O	[16]
nd	1631	Bond vibration O–Co–O	[17]
3649	3649	Stretching vibration O–H	[14]

Note: (T = Si or Al); nd = not detected

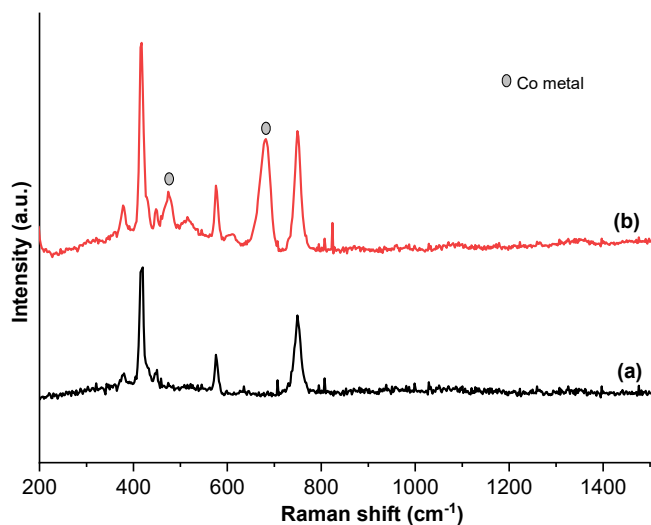


**Fig 4.** Raman spectra of catalysts (a) ZSM-5 and (b) Co/ZSM-5

of microcrystalline  $\text{Co}_3\text{O}_4$  [18-19]. The interaction between oxygen atoms and Co metal affects the movement of oxygen atoms in the plane perpendicular to the 6-membered ring. This statement is indicated by the peak intensity in spectra (b), which is higher than that in spectra (a) in the Raman shift zone of  $376\text{ cm}^{-1}$  belonging to the bending vibration of the 6-membered ring [20]. Metal impregnation was successful because Co was detected in the Raman spectra of Co/ZSM-5. In addition, the higher intensity of the Raman spectra of Co/ZSM-5 means that the amount of light scattered inelastically by the molecule.

The Raman bands of ZSM-5 typically appear in the  $300\text{--}800\text{ cm}^{-1}$  region [21], consistent with the observed peaks at  $376$ ,  $415$ ,  $448$ ,  $576$ ,  $750$ , and  $806\text{ cm}^{-1}$ , which confirm the structural integrity of the ZSM-5 framework. The Raman spectra of Co/ZSM-5 also display broad peaks, similar to those of ZSM-5, reflecting its tetrahedral  $\text{TO}_4$  ( $\text{T} = \text{Si}$  or  $\text{Al}$ ) structure. The vibrations in this range correspond to oxygen motion perpendicular to the  $\text{T-O-T}$  bonds [22-23]. Specifically, the  $376\text{ cm}^{-1}$  peak is assigned to bending vibrations of double six-membered rings, while the  $576$  and  $806\text{ cm}^{-1}$  peaks correspond to symmetric and asymmetric  $\text{T-O-T}$  stretching,

respectively. The enhanced intensity of the  $806\text{ cm}^{-1}$  peak in Co/ZSM-5 indicates an increase in silicalite-rich crystalline regions. The  $415\text{ cm}^{-1}$  band, representing  $\text{O-T-O}$  bending, is the most prominent feature of the ZSM-5 crystalline phase.

#### **Analysis of textural properties of catalysts with the SAA**

Based on size, porous materials are classified into three categories: pores with a diameter  $< 2\text{ nm}$  are called micropores, pores with a diameter of  $2\text{--}50\text{ nm}$  are mesopores, and pores with a diameter  $> 50\text{ nm}$  are macropores [24]. Based on the results presented in Table 3, the ZSM-5 material, both before and after metal impregnation, is mesoporous, with pore diameters ranging from  $2$  to  $50\text{ nm}$ . Information on other aspects, such as material size, also suggests that Co impregnation results in decreases in surface area, total pore volume, and average pore diameter. This can occur because Co metal clogs or blocks some parts of the ZSM-5 pores. The large Co metal particles do not fill the pores of ZSM-5 but only the mesoporous surface. Co metal experiences binding (sintering), which occurs between metal particles due to the heating process of calcination, and is called agglomeration on the surface of the ZSM-5 material. Agglomeration is the combination of metal particles into larger parts, which causes the surface area, total pore volume, and average pore diameter of the ZSM-5 catalyst material to decrease. Agglomerates of metal in the pores of the ZSM-5 surface cause the metal to stick to the pore walls or enter deeper parts and then settle to form a pile of metal [25-26]. In addition, Co metal blocks the large pores of ZSM-5 first, leaving the smaller pores open because ZSM-5 has non-uniform pores. As a result, the average pore diameter decreases.

Textural properties of the catalysts were analyzed using SAA, which generated  $\text{N}_2$  adsorption-desorption isotherm curves (Fig. 5). Both ZSM-5 and Co/ZSM-5 exhibit type IV isotherms with  $\text{H}_2$ -type hysteresis loops,

**Table 3.** Textural properties characterization of ZSM-5 and Co/ZSM-5

Catalyst	Specific surface area ( $\text{m}^2\text{ g}^{-1}$ )	Total pore volume ( $\text{cc g}^{-1}$ )	Average pore diameter (nm)
ZSM-5	263.6	0.181	4.21
Co/ZSM-5	225.1	0.127	3.49

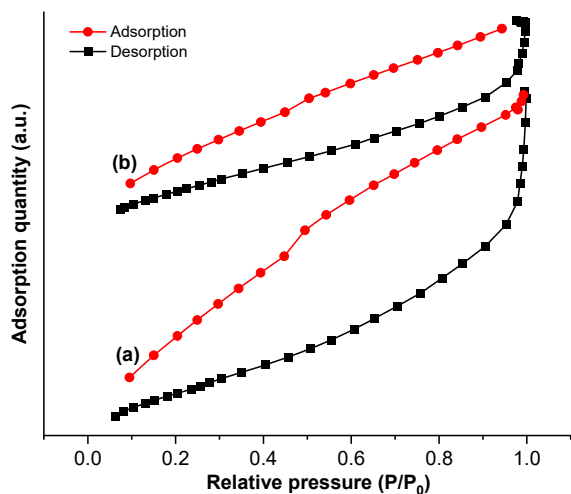


**Fig 5.** Adsorption-desorption isotherm curves of (a) ZSM-5 and (b) Co/ZSM-5 catalysts

characteristic of mesoporous materials with pore diameters in the 2–50 nm range. Compared to ZSM-5, the Co/ZSM-5 curve shows a narrower middle region, indicating a decrease in pore diameter due to metal incorporation. The isotherms increase steadily at relative pressures of 0.2–1.0  $P/P_0$ , reflecting mesoporous capillary condensation and the formation of hysteresis loops caused by delayed condensation under non-equilibrium conditions. The  $H_2$ -type hysteresis suggests the presence of ink-bottle-shaped pores with uneven distribution. In Co/ZSM-5, partial pore blockage by cobalt species restricts  $N_2$  percolation and promotes pore cavitation, further confirming the reduction in pore accessibility.

Based on Fig. 6, it can be seen that the radius of the

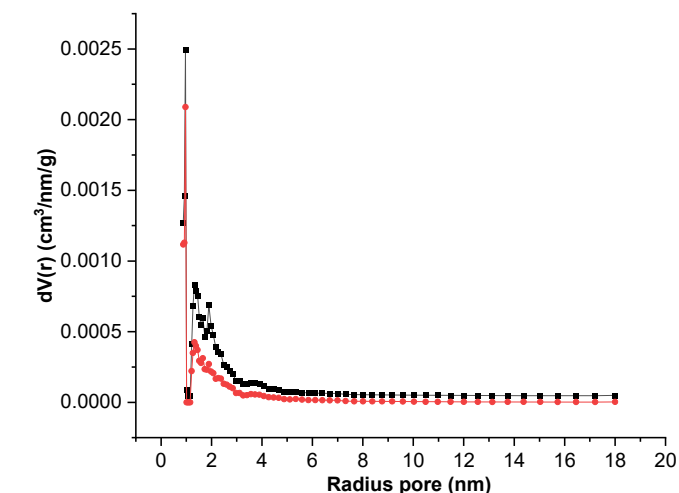
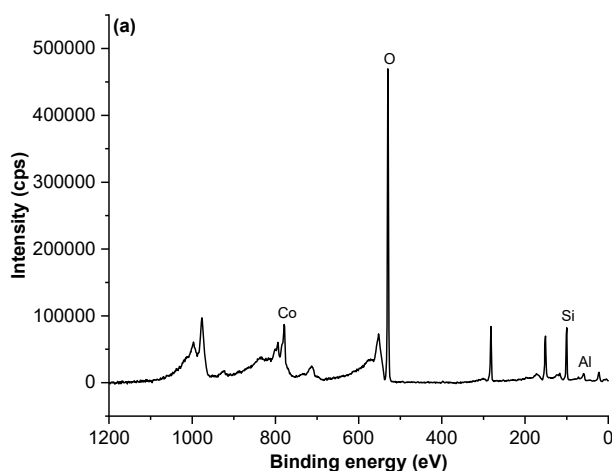


**Fig 6.** Distribution of average pore radius in catalyst (■) ZSM-5 and (●) Co/ZSM-5

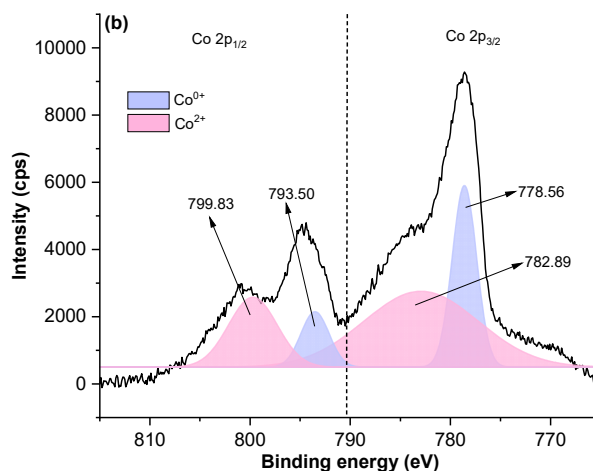


**Fig 7.** XPS spectra of Co/ZSM-5 catalyst (a) wide scan; (b) narrow scan

ZSM-5 and Co/ZSM-5 catalysts falls within the range of 1–18 nm. The dominant pore radius distribution is between 1 and 2 nm. The wide range of pore sizes is likely due to the cobalt impregnation process being carried out without a structure-directing agent or template, such as TPABr or TPAOH, which could otherwise produce more uniform pore sizes. These data are consistent with the adsorption-desorption isotherm curve, confirming that the catalyst material possesses a mesoporous structure.

The sample is in reduced form. The wide scan spectrum of Co/ZSM-5 (Fig. 7) displays signals of Si, O, and Al, consistent with the zeolite (ZSM-5) framework, along with Co metal peaks, confirming the successful

impregnation of Co into the zeolite matrix. The binding energies observed were approximately 77 eV for Al, 100 eV for Si, 531 eV for O, and 780 eV for Co. Oxygen was detected at the 1s level, while Si, Al, and Co were detected at the 2p level. Among these, the most dominant signal originated from oxygen. This strong O 1s peak can be attributed to the formation of cobalt oxides during calcination, to the presence of oxygen in the ambient atmosphere, and to the decomposition of nitrate groups ( $\text{NO}_3^-$ ) in  $\text{Co}(\text{NO}_3)_2$ , which releases additional oxygen. Furthermore, the O 1s peak is also associated with Si–O–Si and Si–O–Al interactions, as previously reported in Raman studies.

To further resolve overlapping peaks, the Co 2p narrow scan spectra were deconvoluted. This analysis revealed the presence of both metallic cobalt ( $\text{Co}^0$ ) and oxidized cobalt ( $\text{Co}^{2+}$ ). Specifically,  $\text{Co}^0$  appeared at  $2p_{3/2} = 778.56$  eV and  $2p_{1/2} = 793.50$  eV, while  $\text{Co}^{2+}$  appeared at  $2p_{3/2} = 782.89$  eV and  $2p_{1/2} = 799.83$  eV. These binding energies fall within the expected Co range of 778–800 eV [27]. The detection of Co species in the high-resolution spectra indicates that Co was successfully introduced into the ZSM-5 structure, consistent with XRD results.

However, the Co remains primarily oxidized, implying incomplete reduction. This difficulty arises not only from the strong interaction between Co and the ZSM-5 framework, which demands harsher reduction conditions, but also from cobalt's inherently very negative reduction potential, making its full reduction to the metallic state particularly challenging.

#### SEM-EDX mapping analysis of ZSM-5 and Co/ZSM-5 catalysts

Based on Fig. 8, Fig. 8(a) and 8(b) show that the gaps between the larger ZSM-5 structures are filled with smaller Co particles, confirming successful metal impregnation without altering the hexagonal structure of ZSM-5 or forming bulk phases. In Fig. 8(c) and 8(d), the morphology of reused catalysts is compared. After three reaction cycles, agglomeration and sintering of the Co particles are observed, resulting in structural damage, particularly in the bottom catalyst, which is more directly exposed to the feed. This accumulation of Co particles reduces the overall catalytic performance.

Based on the catalyst mapping image in Fig. 9, the Co metal dispersion decreased after the catalyst was reused three times. Fig. 9(a) shows that the Co metal

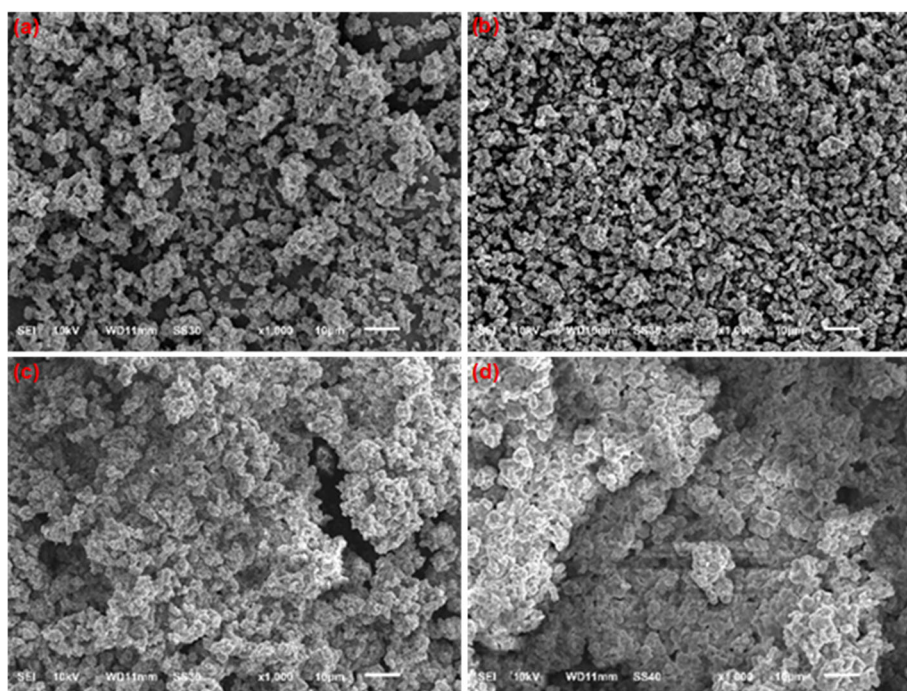


**Fig 8.** Catalyst morphology (a) ZSM-5, (b) Co/ZSM-5 fresh, (c) Co/ZSM-5 spent on top, (d) Co/ZSM-5 spent on bottom

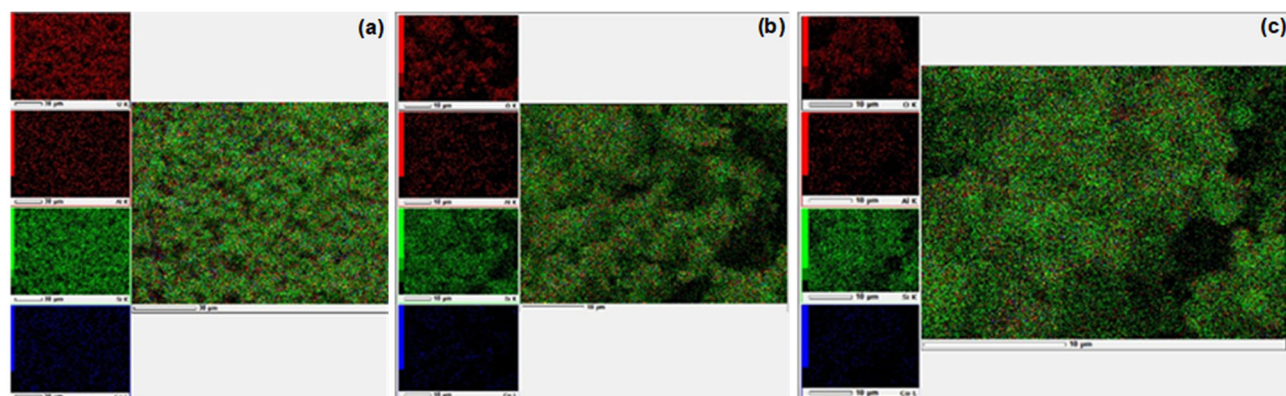


**Fig 9.** Catalyst mapping (a) Co/ZSM-5 fresh, (b) Co/ZSM-5 spent on top, (c) Co/ZSM-5 spent on bottom

distribution remains even because the catalyst has not been used and is still fresh from the impregnation process. However, in points (b) and (c), black holes are visible, and the Co metal mapping is blue. In addition to the decreased Co metal, the mapping also shows a decrease in the abundance of the basic elements of ZSM-5 such as Si, Al, and O. The uneven distribution and sintering of the metal due to the accumulation into larger particles (agglomeration) at one point on the spent catalyst cover the pores of the ZSM-5 carrier, causing a decrease in catalyst activity. An even distribution of metal will affect the active sites on the catalyst surface, thereby increasing the catalyst's activity and selectivity during hydrotreatment. After the mapping and morphology images are presented, the elemental composition of each catalyst is shown in Table 4 and 5.

Based on Table 4, the Co metal composition is appropriate and close to the initial target of 6%. The detected Co metal composition of 5.77% indicates that the metal impregnation, facilitated by ultrasonic waves, was successful. Table 5 shows that the Co metal decreased after the catalyst was used repeatedly three times. The bottom Co/ZSM-5 catalyst after use lost more Co metal than the top one because it was in direct contact during the hydrocracking heating process. In addition, in the catalyst that has been used, there is an apparent increase in the composition of carbon elements, indicating the presence of coke. This is in line with the morphology of the catalyst in Fig. 9. In addition to the presence of metal agglomeration, there is also coke that accumulates and changes the basic structure of ZSM-5.

#### Catalyst acidity test with $NH_3$ -TPD

Based on Fig. 10, the incorporation of Co into ZSM-5 significantly increased the number of strong acid sites

**Table 4.** Percentage composition of fresh ZSM-5 and Co/ZSM-5 catalyst elements

Catalyst	Mass of elements (%)				
	C	Si	O	Al	Co
ZSM-5	0.96	54.24	42.94	1.86	-
Co/ZSM-5	1.39	51.22	39.10	2.52	5.77

**Table 5.** Percentage composition of spent Co/ZSM-5 top and Co/ZSM-5 bottom catalyst elements

Catalyst	Mass of element (%)				
	C	Si	O	Al	Co
Co/ZSM-5 top	6.78	42.68	45.43	1.52	3.59
Co/ZSM-5 bottom	12.99	38.83	43.08	1.82	3.28

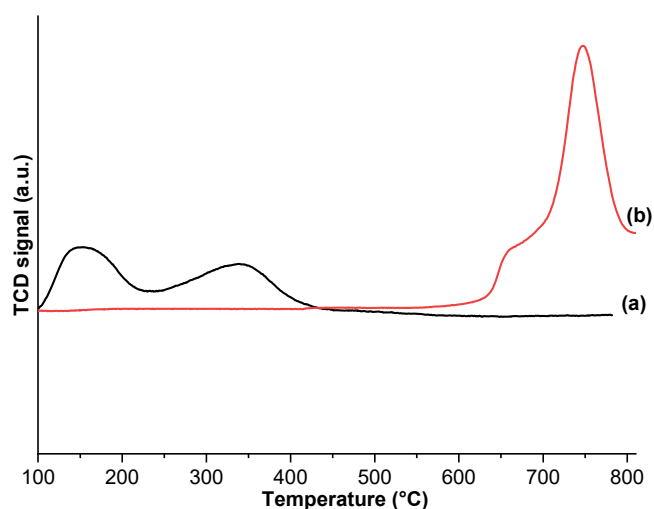


**Fig 10.**  $NH_3$ -TPD analysis curve of catalysts (a) ZSM-5, and (b) Co/ZSM-5

while reducing weak acid sites, as evidenced by the sharper intensity of Co/ZSM-5 compared to pristine ZSM-5 [28]. This confirms the successful impregnation of cobalt, further supported by the homogeneous metal dispersion facilitated by ultrasonic treatment. Weak acid sites were observed at 140–160 and 350–380 °C, while strong acid sites appeared at 650–760 °C. The desorption sequence indicates that weak acid sites are released first, followed by strong acid sites, demonstrating that the acid strength governs the extent of catalyst–reactant interactions.

Table 6 and Fig. 10 show that the total acidity of ZSM-5 (1.398 mmol/g) increased to 2.335 mmol/g after Co impregnation. Initially, the ZSM-5 catalyst exhibited a higher proportion of weak acid sites compared to strong ones. After Co impregnation, the number of strong acid sites increased significantly, while the number of weak acid sites decreased notably. Strong acid sites play a crucial role in initiating hydrotreatment reactions by forming stable complexes with reactant molecules, thereby enhancing the efficiency of bio-jet fuel production.

### Composition Analysis of White Butter (Shortening)

White butter (shortening), a derivative of palm oil, is used as a feedstock for bio-jet fuel production. Its composition was analyzed using GC-MS, revealing 27.26% palmitic acid, 15.35% stearic acid, 40.45% oleic acid, and 12.09% linoleic acid, with a total of 44% saturated fatty acids. The dominant components were palmitic acid (49.34%) and oleic acid (33.91%). These fatty acids undergo hydrodeoxygenation (HDO) during hydrotreatment to remove oxygen and generate bio-jet fuel hydrocarbons within the C<sub>7</sub>–C<sub>16</sub> range. The full fatty acid composition is presented in Table 7.

### Catalyst Application in the Bio-Jet Fuel Formation Process

#### Catalyst activity test of ZSM-5 and Co/ZSM-5

Thermal cracking was carried out to determine the initial temperature at which liquid products appeared.

The first drip temperature decreased after adding metal to the catalyst. As shown in Fig. 11, thermal cracking without a catalyst yielded the lowest conversion, whereas the impregnation of Co into ZSM-5 enhanced catalytic activity and liquid yield. This is supported by acidity analysis, which showed that Co/ZSM-5 has higher total acidity than ZSM-5. Co provides Lewis acid sites, making the catalyst effective for hydrocracking and HDO. The double-bed catalyst arrangement achieved higher conversion than the single-bed configuration because the feed had more frequent and effective contact with the catalyst surface. This improved contact enhanced catalytic activity, resulting in bio-jet fuel yields exceeding 50%. However, catalyst reuse led to a gradual decrease in conversion, attributed to partial loss of active sites and reduced catalytic activity across repeated cycles.

#### Selectivity test of ZSM-5 and Co/ZSM-5 catalysts

The best product from the catalyst arrangement, in the form of a double-bed catalyst, was then analyzed by FTIR. The GC-MS results are categorized into four groups: bio-jet fuel compounds, primary bio-jet fuel compounds, oxygenate compounds, and non-bio-jet fuel compounds. Bio-jet fuel compounds include carbon chains ranging from C<sub>7</sub> to C<sub>16</sub>, including alkanes, alkenes, alkynes, cycloalkanes, cycloalkenes, and aromatic compounds. The primary bio-jet fuel compounds comprise *n*-paraffins, isoparaffins, cycloparaffins, and

**Table 7.** Composition of fatty acids in shortening

Compound name	Compound formula	Area GC (%)
Tetradecanoic acid	C <sub>14</sub> H <sub>27</sub> O <sub>2</sub>	1.23
Hexadecanoic acid	C <sub>16</sub> H <sub>31</sub> O <sub>2</sub>	49.34
Hexadecanoic acid	C <sub>16</sub> H <sub>27</sub> O <sub>2</sub>	8.04
Octadecanoic acid	C <sub>18</sub> H <sub>33</sub> O <sub>2</sub>	33.91
Octadecanoic acid	C <sub>18</sub> H <sub>33</sub> O <sub>2</sub>	0.86
Octadecanoic acid	C <sub>18</sub> H <sub>35</sub> O <sub>2</sub>	5.60

**Table 6.** Results of the acidity level test of ZSM-5 and Co/ZSM-5 catalysts

Catalyst	Acidity (mmol/g)		Total acidity (mmol/g)
	Weak acid site (140–380 °C)	Strong acid site (650–760 °C)	
ZSM-5	1.398	nd	1.398
Co/ZSM-5	nd	2.335	2.335

nd = not detected

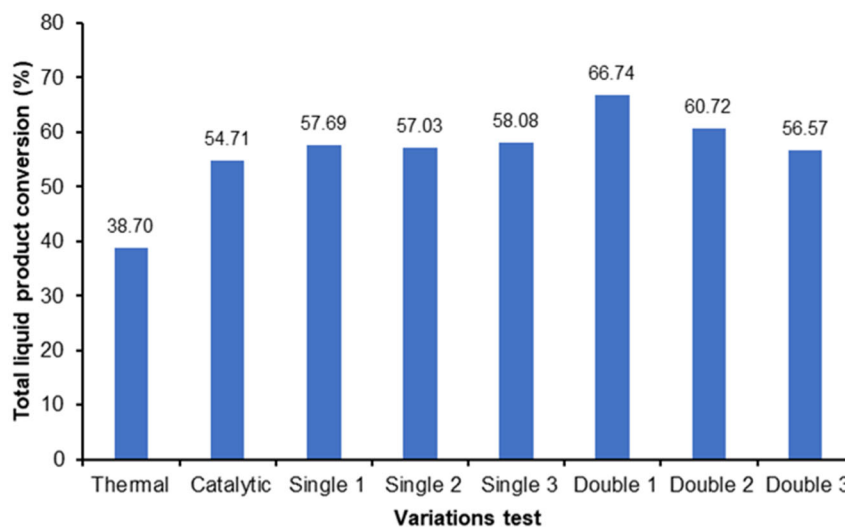


Fig 11. Total diagram of the liquid product conversion of the hydrotreating process

aromatics [19]. Oxygenate compounds consist of alcohol, ketone, carboxylic acid, ester, aldehyde, and other organic compounds that do not react perfectly during the hydrocracking process. Non-bio-jet fuel compounds are hydrocarbons that have a carbon chain of less than 7 and more than 16. The catalyst's selectivity for producing liquid products is presented in Table 8.

Bio-jet fuel compounds dominate the cracking products over oxygenate and non-bio-jet fuel compounds, indicating that the hydrotreatment cracking process is operating quite optimally. Oxygenated products reach up to 20% in runs that do not use catalysts and are not impregnated with metal. After impregnation, the selectivity of oxygenates decreases sharply, indicating that the shortening conversion process has been completed, as oxygenates generally originate from fatty

acids in shortening.

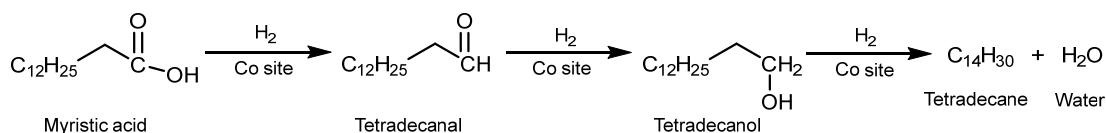
Catalysts with Co impregnation give higher bio-jet fuel yields (Table 9) than ZSM-5 without metal. Catalyst arrangement also matters—double-bed Co/ZSM-5 shows higher yields on the first run due to better stability and stronger feed-catalyst contact. However, yields decrease after three reuses, indicating a reduction in catalytic activity. Co mainly promotes hydrocracking by breaking C–C bonds in triglycerides into free fatty acids. It also contributes to HDO, as evidenced by the reduction in oxygenate compounds (from ~14.93%) after using Co/ZSM-5. Co acts as a Lewis acid site, with unfilled *d* orbitals that can accept electrons. During hydrotreatment, H<sub>2</sub> dissociates homolytically and interacts with Co species (Co, CoO, or Co<sub>3</sub>O<sub>4</sub>), while oxygen atoms facilitate the reaction. In ZSM-5, oxygen

Table 8. Selectivity of liquid products from the shortening hydrotreating process

Run	Total selectivity (%)			
	Bio-jet fuel compounds	Main bio-jet fuel compounds	Oxygenate compounds	Non-bio-jet fuel compound
Thermal	63.22	38.36	20.63	16.96
Catalytic	65.33	44.52	27.29	7.35
Co/ZSM-5 single run 1	84.34	51.05	7.98	8.51
Co/ZSM-5 single run 2	80.92	48.69	9.46	10.31
Co/ZSM-5 single run 3	82.43	43.67	7.83	9.62
Co/ZSM-5 double run 1	78.12	44.50	7.06	16.11
Co/ZSM-5 double run 2	80.00	22.71	8.31	11.47
Co/ZSM-5 double run 3	81.26	53.59	8.01	8.22

**Table 9.** Yield of liquid products from the shortening hydrotreating process

Run	Total yield (%)			
	Bio-jet fuel compounds	Main bio-jet fuel compounds	Oxygenate compounds	Non-bio-jet fuel compound
Thermal	38.70	24.47	7.98	6.56
Catalytic	35.40	24.36	14.93	4.00
Co/ZSM-5 single run 1	48.17	29.45	4.60	4.91
Co/ZSM-5 single run 2	46.15	27.77	5.39	5.88
Co/ZSM-5 single run 3	33.73	25.36	4.55	5.49
Co/ZSM-5 double run 1	51.74	29.47	4.67	10.67
Co/ZSM-5 double run 2	47.43	13.79	5.05	6.96
Co/ZSM-5 double run 3	45.99	30.33	4.53	4.65

**Fig 12.** HDO reaction scheme for the formation of bio-jet fuel compounds

atoms donate electron density, making Al–O bonds weaker and less stable than Si–O bonds. This allows Al to be replaced by –OH, forming Si–OH groups that serve as Brønsted acid sites, which further support catalytic activity.

The hydrocracking mechanism in Fig. 12 occurs by breaking the C–C and C–H bonds of the carbonium ion because there is an acid site from the Co metal, resulting in alkanes (paraffins) and alkenes (olefins). Following this, the hydrodeoxygenation process takes place. The HDO stage comprises hydrogenolysis, dehydration, decarbonylation (DCN) and decarboxylation (DCX), esterification, and transesterification. The reaction began with hydrogenolysis or transesterification, which is used to separate glycerol from fatty acids [20]. Reduction of the carboxyl group to the carbonyl functional group through the C–OH bond. The oxygen atom binds to the active site. Then the active site donates a hydrogen atom to the fatty aldehyde, allowing the oxygen atom to exit the active site as water. The aldehyde will be reduced to a primary alcohol, then hydrogenated to an alkane and water.

The main compounds detected in the bio-jet fuel product are C<sub>14</sub> and C<sub>15</sub>. This is because the feed (shortening) contains high levels of palmitic acid (C<sub>16</sub>) and oleic acid (C<sub>18</sub>), indicating that the hydrotreatment process worked effectively. The carbon distribution of the

hydrocarbon compounds in the liquid product is shown in a histogram based on the number of carbon atoms in Fig. 13. The liquid product demonstrates good selectivity, producing compounds within the bio-jet fuel range, which is strongly influenced by the use of the Co/ZSM-5 catalyst.

Commercial jet-A aviation fuel contains alkane and cycloalkane compounds of 75–85%, the remainder is alkene and aromatic compounds of 25–15% [21]. However, in the conversion results of shortening into bio-jet fuel, there are no aromatic compounds (see Fig. 14). This statement can occur because the application of bio-jet fuel derived from vegetable oil is not 100%, but is still mixed with fossil aviation fuel as much as 5%. The significant presence of olefins in the liquid products originates mainly from the decarbonylation pathway, whereas the formation of paraffins is primarily associated with the decarboxylation reaction. *n*-Alkane compounds (paraffins) are generally preferred for their high stability and energy density. Isoalkanes are especially important because they promote clean combustion, reduce engine-cooling issues, and significantly lower the fuel's freezing point. Cycloalkanes, on the other hand, contribute to high thermal stability. Alkenes (olefins), on the other hand, should be minimized due to their high reactivity and

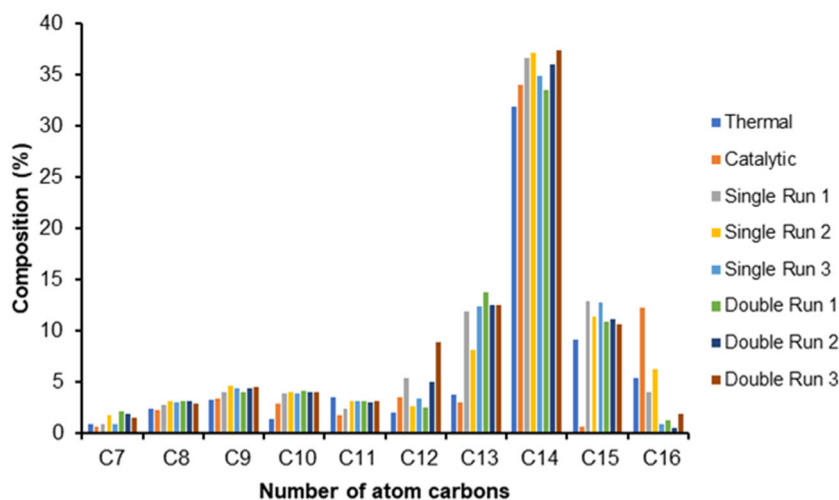


Fig 13. Distribution of the number of carbon atoms in liquid products

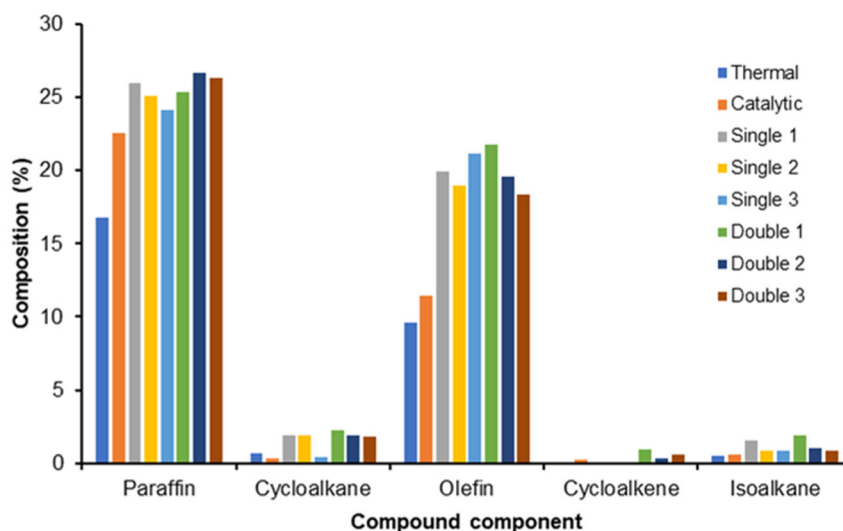


Fig 14. Compound content hydrocarbon of liquid product

tendency to accelerate oxidation during storage.

Although the GC–MS results show a relatively low fraction of isoalkanes, the freezing point of  $-28.20\text{ }^{\circ}\text{C}$  remains relatively low and can be explained by the combined effects of (i) the carbon-number distribution shifted toward lighter hydrocarbons, (ii) the presence of cycloalkanes (naphthenes), and (iii) possible low-level branched isomers that may not be fully resolved by conventional GC analysis but still exert a strong influence on freezing behavior. In addition, trace impurities and residual light oxygenated or unsaturated compounds remaining after hydrotreatment may act as crystallization disruptors, interfering with the orderly packing of *n*-

paraffin molecules and thereby contributing to freezing-point depression. However, this impurity-driven effect is expected to be unstable over the long term. It must be minimized through further upgrading and purification to ensure compliance with ASTM aviation fuel standards.

Commercial aviation fuel (Avtur) obtained from PT Pertamina was analyzed by GC–MS to identify its hydrocarbon composition and to serve as a reference for comparison with the liquid products from the hydrotreatment process (see Fig. 15). The carbon-number distribution of the commercial aviation fuel is presented in Fig. 16. The liquid product obtained from

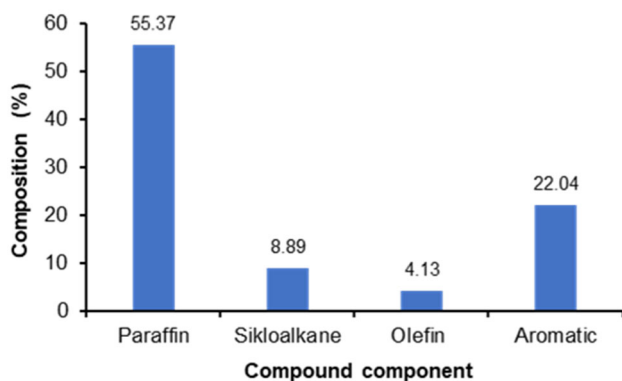


Fig 15. Compound content hydrocarbon in PT Pertamina's commercial avtur

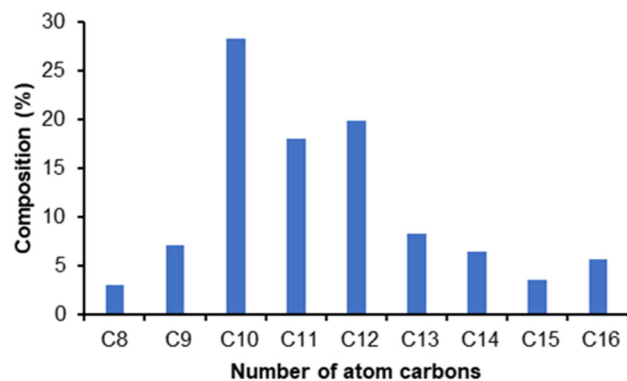


Fig 16. Distribution of the number of carbon atoms in PT Pertamina's commercial avtur

Table 10. Properties of bio-jet fuel product

Properties	Results	Standard	Method
Tf (°C)	-28.20	Max -47	ASTM D2386
Density (kg/m <sup>3</sup> )	776.56	775-840	ASTM D7566-19
API gravity (°)	50.71	38-45	ASTM D7566-19
Kinematic viscosity (mm <sup>2</sup> /s)	1.62	1.3-2.0	ASTM D766
Dynamic viscosity (mPa/s)	1.26	1.3-2.0	ASTM D766

the hydrotreatment process exhibits several properties comparable to those of commercial avtur from PT Pertamina, indicating that the Co/ZSM-5 catalyst performs effectively (Table 10). The bio-jet fuel was evaluated in accordance with ASTM standards. Key properties such as density and viscosity meet the required specifications, ensuring efficient energy utilization and proper fuel flow. However, the freezing point has not yet satisfied the ASTM specification, indicating that the fuel still requires further upgrading to improve its low-temperature operability. Additionally, the API gravity does not meet the ASTM requirement, indicating a relatively high fraction of heavier hydrocarbons (C<sub>13</sub>-C<sub>15</sub>). This suggests that the hydrocarbon distribution still requires optimization to achieve the optimal balance between light and heavy fractions, thereby improving performance and compliance. The use of catalysts in hydrotreatment shortening has successfully enhanced the selectivity of bio-jet fuel [22].

#### FTIR analysis results of bio-jet fuel products with a double-layer catalyst Co/ZSM-5

As presented in Fig. 17, the peak of 1168 cm<sup>-1</sup> only appears in the shortening feed. This indicates that the

HDO reaction is quite successful, as the peak corresponding to the C-O stretching vibration in alcohols, ethers, and carboxylates disappears after the reaction is run in the reactor. The peak at 1739 cm<sup>-1</sup> appears to shorten, and upon hydrotreatment, its intensity decreases, and the wavenumber shifts to 1712 cm<sup>-1</sup>, indicating that the C=O carboxylate group is

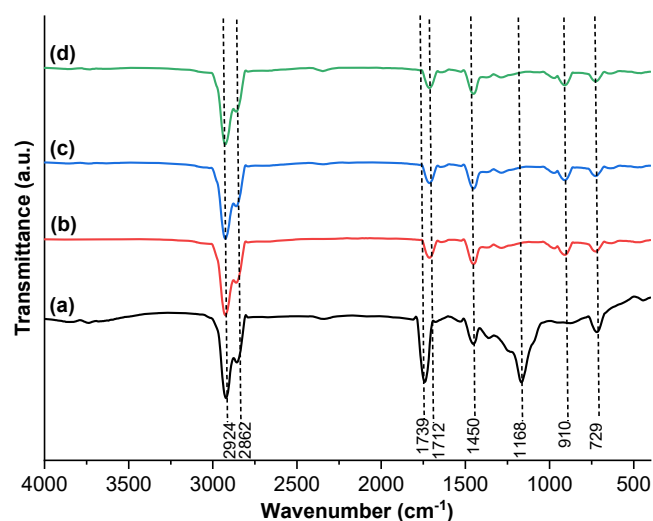


Fig 17. FTIR spectra (a) shortening, (b) run 1, (c) run 2, (d) run 3

**Table 11.** Results of the interpretation of FTIR spectra of feed and product

Wavenumber (cm <sup>-1</sup> )	Types of bonds and vibrations	Reference
729	Rocking $-(CH_2)_n-$ , $n > 4$	[23]
910	Bending C-H alkenes	[24]
1168	Stretching C-O alcohols, ethers, carboxylates	[25]
1450	Stretching C=C alkenes	[26]
1712–1739	Stretching C=O carboxylic acids	[25]
2862–2924	Stretching C-H alkanes	[24]

reduced. The summary of identified functional groups is shown in Table 11.

## ■ CONCLUSION

Based on the results and analysis, the Co/ZSM-5 catalyst was successfully synthesized and exhibited favorable physicochemical properties, including high crystallinity, moderate surface area, a suitable pore structure, and strong acidity. The evaluation of catalytic performance revealed that the arrangement of catalyst beds significantly influenced both conversion efficiency and product yield. The single-bed Co/ZSM-5 catalyst produced a bio-jet fuel yield of 48.17%, while the double-bed configuration achieved a higher yield of 51.74%. In reusability tests over three consecutive cycles, both configurations maintained relatively stable activity, with the double-bed system showing better yield retention (51.74, 47.43, and 45.99%) compared to the single-bed system (48.17, 46.15, and 33.73%). These findings indicate that the double-bed arrangement enhances reaction efficiency and stability, making it a more promising configuration for hydrotreatment-based bio-jet fuel production. The Co distribution analysis further confirmed that the active metal remained well-dispersed after use, with Co contents of 3.59% in the top bed and 3.28% in the bottom bed.

## ■ ACKNOWLEDGMENTS

The authors would like to express their gratitude for the facilities and scientific support from the Physical Chemistry Laboratory, Department of Chemistry, Universitas Gadjah Mada, and also the Nanomaterial Synthesis Laboratory, and material characterization support from the Advanced Characterization Laboratories Serpong and Advanced Physics Imaging

Laboratories Serpong, the National Research and Innovation Agency (BRIN) Indonesia through *E-Layanan Sains*. The authors also acknowledge financial support from the HIBAH MIPA program granted to Prof. Triyono (grant number 3936/UN1/FMIPA.1.3/KP/PT.01.03/2025), which greatly contributed to the completion of this research.

## ■ CONFLICT OF INTEREST

The author declares that each party involved in the research and writing of this journal has no financial conflict of interest or personal relationship that could affect the work presented in this paper.

## ■ AUTHOR CONTRIBUTIONS

Pangestu Arum Pratiwi: Writing–original draft, Research methodology, Data interpretation, Conceptualization, Data analysis. Wega Trisunaryanti: Supervision, Conceptualization, Formal analysis. Triyono: Supervision, Project administration, Funding acquisition. Adyatma Bhagaskara: Writing-original draft, Data interpretation, Instruments. Dita Adi Saputra: Data curation, Investigation. All authors read and agreed to the final version of the manuscript.

## ■ REFERENCES

- [1] Khan, H., Khan, I., and Binh, T.T., 2020, The heterogeneity of renewable energy consumption, carbon emission and financial development in the globe: A panel quantile regression approach, *Energy Rep.*, 6, 859–867.
- [2] Benavides, A., Benjumea, P., Cortés, F.B., and Ruiz, M.A., 2021, Chemical composition and low-temperature fluidity properties of jet fuels, *Processes*, 9 (7), 1184.

- [3] Sulaiman, N.S., Sintang, M.D., Mantihal, S., Zaini, H.M., Munsu, E., Mamat, H., Kanagaratnam, S., Jahurul, M.H.A., and Pindi, W., 2022, Balancing functional and health benefits of food products formulated with palm oil as oil sources, *Heliyon*, 8 (10), e11041.
- [4] Trisunaryanti, W., Wijaya, K., and Tazkia, A.M., 2024, Preparation of Ni/ZSM-5 and Mo/ZSM-5 catalysts for hydrotreating palm oil into bio-jet fuel, *Commun. Sci. Technol.*, 9 (1), 161–169.
- [5] Vásquez, M.C., Silva, E.E., and Castillo, E.F., 2017, Hydrotreatment of vegetable oils: A review of the technologies and its developments for jet biofuel production, *Biomass Bioenergy*, 105, 197–206.
- [6] Li, C., Han, Y., Yang, T., and Deng, W., 2020, Preliminary study on the influence of catalyst dosage on coke formation of heavy oil slurry-bed hydrocracking, *Fuel*, 270, 117489.
- [7] Rambabu, K., Bharath, G., Sivarajasekar, N., Velu, S., Sudha, P.N., Wongsakulphasatch, S., and Banat, F., 2023, Sustainable production of bio-jet fuel and green gasoline from date palm seed oil via hydroprocessing over tantalum phosphate, *Fuel*, 331 (Pt. 1), 125688.
- [8] Li, R., Huang, D., Wei, Z., Chen, Y., Wang G., Zhou, W., Xiao, R., and Xu, W., 2025, Synthesis of biomass-mediated hierarchical Zeolite Socony Mobil-5 and their selectivity for lignin conversion to bio-oils: Review and perspective, *Renewable Sustainable Energy Rev.*, 207, 114977.
- [9] Wang, C., Wang, Y., Chen, M., Hu, J., Liang, D., Tang, Z., Yang, Z., Wang, J., and Zhang, H., 2021, Comparison of the regenerability of Co/sepiolite and Co/Al<sub>2</sub>O<sub>3</sub> catalysts containing the spinel phase in simulated bio-oil steam reforming, *Energy*, 214, 118971.
- [10] Rahmawati, Z., Santoso, L., McCue, A., Azua Jamari, N.L., Ninglasari, S.Y., Gunawan, T., and Fansuri, H., 2023, Selectivity of reaction pathways for green diesel production towards biojet fuel applications, *RSC Adv.*, 13 (20), 13698–13714.
- [11] Trisunaryanti, W., Triyono, T., Nugrahagusti, I.H., and Purbonegoro, J., 2025, Effect of nickel precursor salt variation in Ni/mesoporous carbon catalyst synthesis from teak sawdust waste for microwave-assisted hydrocracking of castor oil into biofuel, *Waste Biomass Valorization*, 16 (9), 5037–5052.
- [12] Ameen, M., Azizan, M.T., Ramli, A., Yusup, S., and Alnarabiji, M.S., 2019, Catalytic hydrodeoxygenation of rubber seed oil over sonochemically synthesized Ni-Mo/ $\gamma$ -Al<sub>2</sub>O<sub>3</sub> catalyst for green diesel production, *Ultrason. Sonochem.*, 51, 90–102.
- [13] Shilina, M., Krotova, I., Nikolaev, S., Gurevich, S., Yavsin, D., Udalova, O., and Rostovshchikova, T., 2023, Highly effective Pt-Co/ZSM-5 catalysts with low Pt loading for preferential CO oxidation in H<sub>2</sub>-rich mixture, *Hydrogen*, 4 (1), 154–173.
- [14] Aziz, A., Sajjad, M., Kim, M., and Kim, K.S., 2018, An efficient Co-ZSM-5 catalyst for the abatement of volatile organics in air: Effect of the synthesis protocol, *Int. J. Environ. Sci. Technol.*, 15 (4), 707–718.
- [15] Basir, M.N., Jamil, N.A.M., and Hamdan, H., 2021, Conversion of jet biofuel range hydrocarbons from palm oil over zeolite hybrid catalyst, *Nanomater. Nanotechnol.*, 11, 1847980420981536.
- [16] Jia, Y., Shi, Q., Wang, J., Ding, C., and Zhang, K., 2020, Synthesis, characterization, and catalytic application of hierarchical nano-ZSM-5 zeolite, *RSC Adv.*, 10 (50), 29618–29626.
- [17] Bellmann, A., Atia, H., Bentrup, U., and Brückner, A., 2025, Mechanism of the selective reduction of NO<sub>x</sub> by methane over Co-ZSM-5, *Appl. Catal., B*, 230, 184–193.
- [18] Pierella, L.B., Saux, C., Caglieri, S.C., Bertorello, H.R., and Bercoff, P.G., 2008, Catalytic activity and magnetic properties of Co-ZSM-5 zeolites prepared by different methods, *Appl. Catal., A*, 347 (1), 55–61.
- [19] Bhagaskara, A., Saputra, D.A., Trisunaryanti, W., Wijaya, K., Rozana, K., Susanto, H., Pradana, R.A.P., Hartanto, H.D., Lallasari, L.H., and Prasetyo, A.B., 2026, Investigation of reaction mechanism in selective citric acid leaching of Ni and Co from NMC cathodes via real time Raman spectroscopy and RSM optimization, *J. Indian Chem. Soc.*, 103 (2), 102410.

- [20] Bhagaskara, A., Trisunaryanti, W., Wijaya, K., Meylida Tazkia, A., Adi Saputra, D., Marantha Haryanto, V., Arfiana, A., and Zainuddin, I., 2026, Valence state-dependent catalytic behavior of Ni and Co in NiCo/activated carbon derived from spent Li-ion batteries for bio-jet fuel production, *J. Indian Chem. Soc.*, 103 (2), 102413.
- [21] Doliente, S.S., Narayan, A., Tapia, J.F.D., Samsatli, N.J., Zhao, Y., and Samsatli, S., 2020, Bio-aviation fuel: A comprehensive review and analysis of the supply chain components, *Front. Energy Res.*, 8, 110.
- [22] Trisunaryanti, W., Wijaya, K., and Saputro, M.D.I., 2025, The effect of Ni/AC and Mo/AC catalyst arrangements on the activity and selectivity for hydrotreating palm cooking oil into biojet fuel, *Indones. J. Chem.*, 25 (2), 404–419.
- [23] Redda, Z.T., Laß-Seyoum, A., Yimam, A., Barz, M., and Jabasingh, S.A., 2022, Solvent extraction and characterization of *Brassica carinata* oils as promising alternative feedstock for bio-jet fuel production, *Biomass Conv. Bioref.*, 14 (11), 12207–12226.
- [24] Sarjadi, M.S., Ling, T.C., and Khan, M.S., 2019, Analysis and comparison of olive cooking oil and palm cooking oil properties as biodiesel feedstock, *J. Phys.: Conf. Ser.*, 1358 (1), 012007.
- [25] Carli, M.F., Susanto, B.H., and Habibie, T.K., 2018, Sythesis of bioavture through hydrodeoxygenation and catalytic cracking from oleic acid using NiMo/zeolit catalyst, *E3S Web Conf.*, 67, 02023.
- [26] da Rocha Novaes, L., Secchi, A.R., Salim, V.M.M., and de Resende, N.S., 2022, Enhancement of hydrotreating process evaluation: Correlation between feedstock properties, in-line monitoring and catalyst deactivation, *Catal. Today*, 394-396, 390–402.
- [27] Bhagaskara, A., Saputra, D.A., Saviola, A.J., Wijaya, K., Oh, W.C., Rahayu, S., Gumelar, M.D., Saudi, A.U., Agustanhakri, A., Budiman, A.H., and Indrijarso, S., 2024, Recycling of nickel metal from spent nickel-manganese-cobalt (NMC) cathode batteries using  $\text{H}_3\text{PO}_4\text{-H}_2\text{C}_2\text{O}_4$  solution combination as an efficient leaching agent, *Case Stud. Chem. Environ. Eng.*, 10, 100844.
- [28] Bhagaskara, A., Wijaya, K., Trisunaryanti, W., Saputra, D.A., Agustanhakri, A., Taqwatomo, G., Arjasa, O.P., Budiman, A.H., and Anggaravidya, M., 2025, Upcycling secondary nickel from spent nickel-manganese-cobalt (NMC) batteries as a nanocatalysts on sulfated natural zeolite for converting LDPE plastic waste into jet-fuel hydrocarbons, *Next Mater.*, 9, 101107.